Comput. Methods Appl. Mech. Engrg. 200 (2011) 2768–2781

Contents lists available at ScienceDirect

Comput. Methods Appl. Mech. Engrg.

journal homepage: www.elsevier.com/locate/cma

A posteriori error analysis for a cut cell finite volume method

Don Estep [a,b], Michael Pernice [c], Simon Tavener [a], Haiying Wang [d,*]

[a] Department of Mathematics, Colorado State University, Fort Collins, CO 80523, USA
[b] Department of Statistics, Colorado State University, Fort Collins, CO 80523, USA
[c] Idaho National Laboratory, Idaho Falls, ID 83415, USA
[d] Department of Mathematical Sciences, Michigan Technological University, Houghton, MI 49931, USA

ARTICLE INFO

Article history:
Received 23 December 2009
Received in revised form 30 July 2010
Accepted 22 November 2010
Available online 26 November 2010

Keywords:
Cut cell problem
Discontinuous diffusion
A posteriori error analysis
Adjoint problem
Finite volume method
Modeling error

ABSTRACT

We study the solution of a diffusive process in a domain where the diffusion coefficient changes discontinuously across a curved interface. We consider discretizations that use regularly-shaped meshes, so that the interface "cuts" through the cells (elements or volumes) without respecting the regular geometry of the mesh. Consequently, the discontinuity in the diffusion coefficients has a strong impact on the accuracy and convergence of the numerical method. This motivates the derivation of computational error estimates that yield accurate estimates for specified quantities of interest. For this purpose, we adapt the well-known adjoint based *a posteriori* error analysis technique used for finite element methods. In order to employ this method, we describe a systematic approach to discretizing a cut-cell problem that handles complex geometry in the interface in a natural fashion yet reduces to the well-known Ghost Fluid Method in simple cases. We test the accuracy of the estimates in a series of examples.

1. Introduction

1.1. Elliptic problems with discontinuous diffusion coefficients and "cut-cell" discretizations

In this paper, we consider the solution of a diffusive process:

$$\begin{aligned} -\nabla\cdot(a\nabla p) &= f, \quad \text{in } \Omega, \\ p &= g, \quad \text{on } \partial\Omega, \end{aligned} \tag{1}$$

in a convex polyhedral domain $\Omega \in \mathbb{R}^2$ with boundary $\partial\Omega$ that consists of two distinct materials with different material properties, see Fig. 1.1. We assume that the diffusion value changes discontinuously across a smooth interface curve Γ_d interior to Ω, while we require that the solution be continuous and have a continuous normal flux across the interior interface boundary. Specifically, we assume that a is smooth in each sub-domain of Ω determined by Γ_d, a has one-sided limits at Γ_d, and $a(\mathbf{x})$ is bounded below by a positive number. We also assume that $f \in L^2(\Omega)$ and $g \in H^{1/2}(\partial\Omega)$. Finally, we assume $p \in W = L^2(\Omega)$ and $\mathbf{u} = -a\nabla p \in \mathbf{V} = \mathrm{H}(\mathrm{div};\Omega) = \{\mathbf{v} \in (L^2(\Omega))^2 : \mathrm{div}\,\mathbf{v} \in L^2(\Omega)\}$. Such problems arise in many contexts, e.g. biology, chemistry, material science, and fluid flow. The particular problem motivating this work is heat conduction in nuclear fuel rods consisting of an uranium core and a steel cladding.

Elliptic problems with discontinuous diffusion coefficients pose well known challenges for reliably accurate numerical solution because of the difficulties arising from the discontinuity. Consequently, this is a very active area of numerical analysis in which a number of approaches are being pursued, e.g. special discretization methods, adaptive mesh refinement, embedded interface methods, and so forth. The difficulties are magnified significantly when the interface has complex geometry that is not aligned with a discretization mesh and when the coefficient is not piecewise constant. Generally in this case, loss of order of accuracy is expected and numerical error in computed results is always significant. Consequently, obtaining *accurate* estimates of the error in a quantity of interest computed from a given numerical solution is critically important in practical applications regardless of the particular numerical approach. This provides the basic motivation for the work in this paper.

In many application domains involving diffusive and transport problems, there is a strong preference towards the use of locally conservative methods, e.g. finite volume as well as special discontinuous Galerkin and mixed finite element methods, even at the cost of relatively low order of accuracy for some common methods. Since locally conservative schemes are generally easier to construct and implement on regularly-shaped discretizations,

* Corresponding author. Tel.: +1 906 487 2099; fax: +1 906 487 3133.
E-mail address: haiyingw@mtu.edu (H. Wang).

0045-7825/$ - see front matter © 2010 Elsevier B.V. All rights reserved.
doi:10.1016/j.cma.2010.11.015

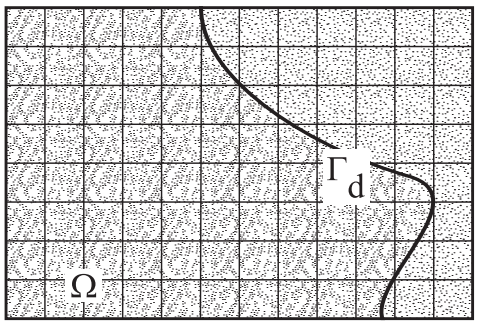

Fig. 1.1. Two adjoining materials with different diffusion properties. The smooth interface cuts through the cells of a regular discretization.

there are several well known approaches for problems with discontinuous coefficients that employ regularly-shaped discretizations, so that the interface cuts through the discretization cells, yielding a "cut-cell" problem.

In this paper, we study the well known "Ghost Fluid Method" for discontinuous interface problems [1,2]. The Ghost Fluid Method is a special finite volume method introduced for the related problem in which flux and state may be discontinuous across the interface. The Ghost Fluid Method yields a locally conservative finite volume scheme that approximates discontinuous solutions without oscillations near the interface. It has been successfully used in a wide range of applications, including spray atomization [3,4], droplet dynamics [5–7], combustion [8,9], vaporization at reactive interfaces [10,11], bubbly flows [12], alumina electrolysis [13], and visualization of fluid flow [14,15]. These applications all implement the level set method [16] to describe a sharp interface between fluid states and to track complex topological changes of the interface.

Alternatively, one could employ discretizations that are matched to the interface. However, such methods also face considerable technical difficulties in analysis and implementation. In particular, generating high quality unstructured and body-fitted multi-block grids for complex interface geometries is not yet fully automated, and can consume a large fraction of the time to perform a simulation. On the other hand, generating a cut-cell representation of an interface is much faster and generally more robust, since it relies on solving local intersection problems, a procedure that is fully automated [17]. Moreover, there are situations that suggest the use of regular discretizations, e.g.

- Evolution problems in which the interface is evolving, perhaps dependent on the behavior of the solution, in which case repeatedly generating meshes to match the evolving interface is expensive.
- Problems in which the interface is determined from experimental measurement and is described with relatively poor accuracy, in which case using a high resolution representation is not justified.
- Sensitivity analysis studies involving the solution of many interface problems with varying interfaces, in which case it may be desirable to minimize the cost of each sample solution.
- Problems in which the quantities of interest to be computed from the model are relatively insensitive to the exact location of the interface.

1.2. The connection between finite volume and finite element methods and accurately estimating the error in a cut-cell discretization

Producing accurate estimates of numerical error in computed results for a discontinuous interface problem is a practically important issue, e.g. for uncertainty quantification. *A priori* convergence analysis for a cut-cell discretization is problematic and the results, typically involving loss of order, are discouraging. Indeed, for the general situation, the convergence analysis does not yield an order of convergence, see [2].

Instead, we take a different approach to error estimation by deriving a computational error estimate that provides a way to compute an accurate estimate of the error in a quantity of interest during an actual computation. For this purpose, we adapt a powerful *a posteriori* error analysis technique well-known in the finite element community. This approach [18–23] uses an adjoint problem, computable residuals, and variational analysis to produce a computational estimate of the error in a quantity of interest determined by a specified linear functional of the solution. The resulting estimate is generally accurate and is also precise in the sense of decomposing the error into contributions from various sources, taking into account the full effects of stability on accumulation, cancellation, and propagation of errors.

This *a posteriori* approach is based on variational analysis, which makes it natural for a finite element discretization. To apply the method to a finite difference or finite volume discretization, these discretizations are described as a particular kind of finite element method employing specialized quadrature formulas inside cells to evaluate integrals in the weak form of the differential equation. For example, there is a well-known equivalence between mixed finite element methods employing special basis functions and quadrature formulas and cell-centered finite volume methods [18,24–26]. We use this in [18] to derive *a posteriori* error estimates for cell-centered finite volume methods for elliptic problems.

It is straightforward to use this approach when the interface aligns with the cell boundaries in the discretization mesh. In particular, there are no theoretical issues in using quadrature to evaluate integrals involving the diffusion coefficient inside mesh cells. However, a cut-cell problem is problematic because the use of quadrature formula across a cell in which the diffusion parameter is discontinuous is not justified theoretically. Likewise, actually computing the integrals exactly when there is a complex interface geometry inside a cell is very problematic. See [27] for a recent overview of approaches for treating this lack of smoothness. Thus, a second major goal of this paper is deriving a systematic approach to finite element discretization that applies to general cut-cell discretizations, reduces to the Ghost Fluid Method in simple cases, and allows the application of *a posteriori* error analysis. We stress that our interest lies in the general problem of an interface for non-constant coefficient diffusion with complex geometry that does not align with the discretization. It is generally problematic to extend standard approaches for treating discontinuous interface problems based on simplifying assumptions, such as interfaces that align with cell boundaries.

Our approach to a cut-cell finite element method involves two steps. First, we replace, or "model", the discontinuous diffusion coefficient with a piecewise polynomial function (linear in one dimension and biquadratic in two dimensions) in a relatively small region Ω_d containing the interface Γ_d that scales with the mesh. The approximation is continuous in Ω_d. This essentially "spreads" the discontinuity to the boundary of Ω_d, so that the lack of smoothness of the new model coefficient is restricted to cell boundaries. After this, we choose an appropriate basis and quadrature formula to obtain a finite volume scheme that is equivalent to the Ghost Fluid Method in simple cases.

To describe this in a simple case, consider a one dimensional problem with a piecewise constant diffusion where the discontinuity is located at a point x_* in the interior of a cell, see Fig. 2.1. The Ghost Cell approximation is determined by a standard finite volume method applied to a *new* model problem in which the value

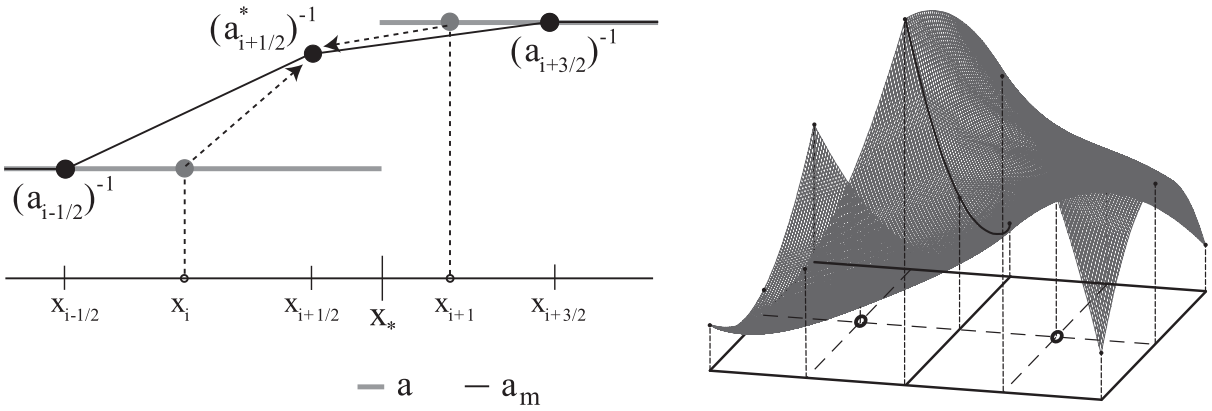

Fig. 2.1. Left: We illustrate the computation of the weighted harmonic average in the case of a piecewise constant diffusion function. The discontinuity is at x_*. The weighted harmonic average value $a^*_{i+1/2}$ at $x_{i+1/2}$ is determined by the values at the cell centers x_i, x_{i+1} containing x_* weighted by the distances from x_* to the cell centers. We also plot the piecewise linear continuous model diffusion $a_m(x)$ in one dimension. a and a_m agree outside the interval $\Omega_d = [x_{i-1/2}, x_{i+3/2}]$. Right: The continuous, piecewise biquadratic model diffusion coefficient in two dimensions for a typical problem. The vertical lines indicate the nodal points for the biquadratic interpolation. The smoothness within cells and the continuity across the cell boundary is evident.

of the diffusion at the cell boundary point closest to the discontinuity x_* is altered to be a weighted version of the harmonic average $\left(\frac{1}{2}(\frac{1}{a}+\frac{1}{b})\right)^{-1}$ of the values a and b at two points. We discuss the weighted harmonic average (3) and its importance for discontinuous interface problems below.

We note that there generally is no unique way to write a given finite volume method as an equivalent finite element method. In the course of deriving the method presented in this paper, we derived a number of approaches for the Ghost Fluid Method. However, the approach described in this paper deals naturally with some geometric issues that arise in two dimensions and allows for computation of accurate *a posteriori* error estimates. As mentioned, our approach involves "smearing" or smoothing the discontinuity on the interface so that any lack of smoothness in the model diffusion lies on the cell boundaries of the small region Ω_d. This region shrinks with the mesh size, and the model coefficient converges to the true coefficient as the mesh is refined.

A key point is that the Ghost Fluid Method involves both a modeling step-in the form of altering the value of the diffusion in a small region-and a discretization step-in the form of mixed finite element method with special quadrature. Both steps contribute significantly to the error of the method. In this application, we show how to modify the standard analysis for a mixed finite element/finite volume method [18] to account for the modeling error in the cut-cell finite element method. This provides the tools to estimate the relative contributions to the error from modeling and discretization.

The *a posteriori* error analysis used in this paper can be carried out generally for a wide range of discretizations. The critical step is to identify the two key ingredients: (1) modeling the diffusion and (2) introducing an appropriate mixed finite element or discontinuous Galerkin method.

1.3. Outline of the paper

The outline of the paper is as follows. In Section 2, we describe the discretization. We present the results of an analysis of the modeling error along with a goal-oriented *a posteriori* error analysis in Section 3 while the proofs are presented in Appendix A. In Section 4, we present a series of numerical examples. In Section 5, we present an analysis of the effects of error in the location of the interface. In Section 6, we present the conclusion.

2. Construction of the discrete approximation

Recall that the goal is to construct a finite element discretization that is equivalent to the Ghost Fluid Method in simple cases, yet allows treatment of interfaces with complex geometry and non-constant diffusion coefficients. We discretize (1) using a two step process. We first replace (1) by a "model" problem. Then, we discretize the model problem using a mixed finite element method.

2.1. Construction of the model problem

The first step in the discretization is to replace (1) by a model problem:

$$\begin{aligned} -\nabla\cdot(a_m\nabla p) &= f, \quad \text{in } \Omega \\ p &= g, \quad \text{on } \partial\Omega, \end{aligned} \tag{2}$$

where we replace $a \approx a_m$. To define a_m, we use a weighted harmonic average computed along lines. Consider a canonical interval Ω on a line. The line contains the problem domain in one dimension and joins neighboring cell centers in two dimensions. We assume that the interval has been discretized using a partition $\{[x_{j-1/2}, x_{j+1/2}], j = 1,2,\ldots,N\}$, with cell boundaries located at $\{x_{j+1/2}, j = 0,1,\ldots,N\}$, cell centers $\{x_j, j = 1,2,\ldots,N\}$, and $\Omega = [x_{1/2}, x_{N+1/2}]$. We suppose the discontinuity is located at $x_* \in [x_i, x_{i+1}]$, see Fig. 2.1. We define the weighted harmonic average $a^*_{i+1/2}$ of the values of a at $x_{i+1/2}$ to be:

$$a^*_{i+1/2} = \left(\frac{\gamma}{a_i} + \frac{1-\gamma}{a_{i+1}}\right)^{-1}, \tag{3}$$

where $a_i = a(x_i), a_{i+1} = a(x_{i+1})$ and $\gamma = (x_* - x_i)/(x_{i+1} - x_i)$. That is, $a^*_{i+1/2}$ is a harmonic average weighted by the fractions of the sub-domain over which a takes its different values.

2.1.1. Construction of a_m in one dimension

Our focus is on the two dimensional case, but the one-dimensional case is illustrative. We define a model problem in which discontinuous diffusion coefficient $a(x)$ is replaced by a continuous piecewise linear approximation $a_m(x)$ that interpolates a at $x_{i-1/2}$ and $x_{i+3/2}$ and has value equal to the weighted harmonic average at $x_{i+1/2}$. This means that we alter the value of a to obtain a_m in the region $\Omega_d = [x_{i-1/2}, x_{i+3/2}]$, and set $a_m \equiv a$ in the complement. On $\Omega_d, a_m(x)$ is given by

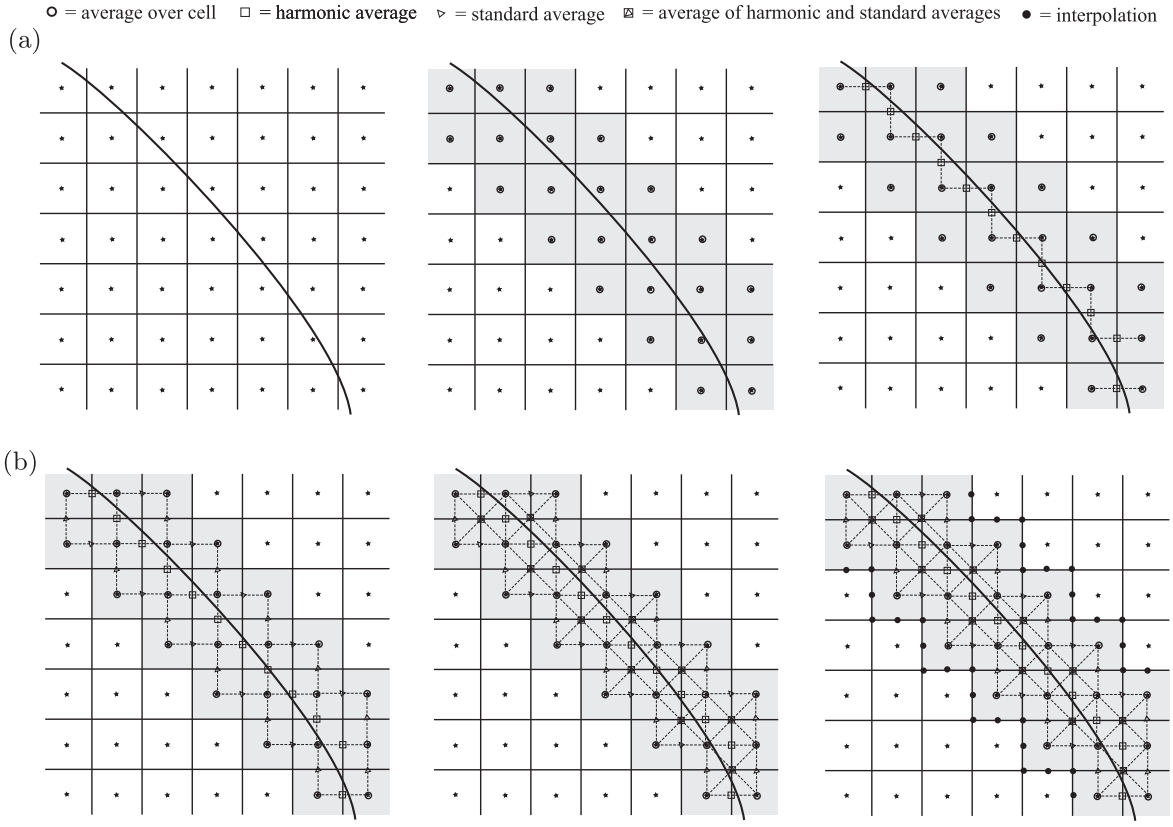

Fig. 2.2. Illustration of Algorithm 1. (a) Left: Beginning with an interface and a discretization. Middle: We identify the modeling region and set values at the cell centers for cells in the region. Right: We then compute harmonic averages at the appropriate cell boundary centers. (b) Left: We compute standard averages at the other interior cell boundary centers. Middle: We use appropriate averages of harmonic and standard averages determined along the diagonal collinear connecting line segments between cell centers to determine values at interior cell nodes. Right: We use interpolation to assign the remaining values on the boundary of the modeling region.

$$a_m^{-1}(x) = \begin{cases} \dfrac{\left(a^*_{i+1/2}\right)^{-1} - \left(a_{i-1/2}\right)^{-1}}{x_{i+1/2} - x_{i-1/2}}\left(x - x_{i-1/2}\right) + \left(a_{i-1/2}\right)^{-1}, \\ \quad x \in \left[x_{i-1/2}, x_{i+1/2}\right], \\ \dfrac{\left(a_{i+3/2}\right)^{-1} - \left(a^*_{i+1/2}\right)^{-1}}{x_{i+3/2} - x_{i+1/2}}\left(x - x_{i+3/2}\right) + \left(a_{i+3/2}\right)^{-1}, \\ \quad x \in \left[x_{i+1/2}, x_{i+3/2}\right], \end{cases}$$

where $a^*_{i+1/2}$ is the weighted harmonic average (3). We illustrate $a_m^{-1}(x)$ in Fig. 2.1.

2.1.2. Construction of a_m in two dimensions

It is problematic to extend the one dimensional model approximation directly to two dimensions because of increased geometric complexity. In one dimension, cell centers are connected collinearly through a cell node, while in two dimensions, cell centers are connected collinearly through a cell boundary at the cell boundary center. Consequently, we treat cell boundary centers and cell nodes differently in two dimensions.

To create the model coefficient, we again use the weighted harmonic average (3), but now applied on various line segments that connect cell centers in neighboring cells that share a common cell boundary or a common cell node diagonally. We discretize the canonical two-dimensional domain Ω which we take to be a unit square. We partition Ω in the x and y-directions as

$$0 = x_{1/2} < x_1 < x_{3/2} < x_2 < \cdots < x_{k-1/2} < x_k < x_{k+1/2} = 1,$$
$$0 = y_{1/2} < y_1 < y_{3/2} < y_2 < \cdots < y_{\ell-1/2} < y_\ell < y_{\ell+1/2} = 1.$$

We then define the cells (finite volumes) to be the rectangles:

$$K_{ij} = \left(x_{i-1/2}, x_{i+1/2}\right) \times \left(y_{j-1/2}, y_{j+1/2}\right), \quad i = 1, \ldots, k, \ j = 1, \ldots, \ell$$

with the centers (x_i, y_j) and nodes of half indices. We set:

$$\Delta x_{i+1/2} = x_{i+1} - x_i, \quad i = 1, \ldots, k-1;$$
$$\Delta x_i = x_{i+1/2} - x_{i-1/2}, \quad i = 1, \ldots, k;$$
$$\Delta y_{j+1/2} = y_{j+1} - y_j, \quad j = 1, \ldots, \ell - 1;$$
$$\Delta y_j = y_{j+1/2} - y_{j-1/2}, \quad j = 1, \ldots, \ell.$$

The discrete mesh Ω_h is then defined as $\Omega_h = \{K_{ij}, i = 1, \ldots, k; j = 1, \ldots, \ell\}$.

To determine a model diffusion coefficient, we construct a region Ω_d using discretization volumes that contain the interface curve Γ_d in the interior together with discretization volumes that share a cell boundary with one of these cut cells. We alter the value of a to obtain a_m in the region Ω_d and set $a_m \equiv a$ in the complement. We choose the model coefficient a_m to be a continuous piecewise biquadratic function on Ω_d, with interpolation points at the four cell nodes (vertices), the four cell boundary centers and at the cell center. This construction is illustrated for a pair of adjacent cells in Ω_d in Fig. 2.1. The values of the coefficients for the model problem at nodes and cell faces are determined according to Algorithm 1 and a piecewise biquadratic surface is then fit to this data. Clearly numerical cell-by-cell quadrature formulae are now well behaved for the model problem.

We describe the procedure for constructing a_m in Algorithm 1. The Algorithm is illustrated in Fig. 2.2.

Algorithm 1: Construction of the cut-cell model diffusion coefficient

1. *Determine Ω_d.* Identify the cut cells containing the interface Γ_d. Add those cells that share a cell boundary with the cut cells to obtain Ω_d. Determine the location and orientation of the interface with respect to each cut cell center
2. *Set values at cell centers in Ω_d.* In case the diffusion is constant in a cell, use that constant value. If the diffusion varies over a cell, use the integral average over the cell
3. *Set values at cell boundary midpoints in Ω_d.* For a cell boundary midpoint that lies on a line segment connecting a pair of cell centers in Ω_d, use the weighted harmonic average (3) of the cell center values if the line segment connecting the cell centers is cut by the interface, otherwise use the regular average of the cell center values
4. *Set values at cell nodes in Ω_d.* We compute two values for each cell node and then we average to obtain the value for the cell node. Each value is obtained by averaging cell center values for each pair of cell centers that lie on a diagonal line segment through the cell node. We use the weighted harmonic average (3) when the interface cuts through the diagonal line segment joining the two cell centers. Otherwise, we use the regular average
5. *Set the values at the remaining interpolation points in Ω_d.* Use interpolation to set any remaining values in the interpolation points for the piecewise biquadratic model diffusion, e.g. at points located on the boundary of Ω_d

Note that in two dimensions, we replace the interface of the discontinuity in a by a "stepwise" interface $\partial\Omega_d$ which is comprised of cell boundaries while the diffusion is replaced in a region bounded by the new interface. Since Ω_d scales with the mesh size, the model diffusion converges to the true diffusion as the mesh is refined.

2.2. Discretization of the model problem

With the introduction of a model diffusion that re-locates any discontinuity to cell boundaries, we can now discretize the model problem using a mixed finite element method implemented with a specially chosen quadrature that yields a cell-centered finite volume scheme [18,24–26]. We set $\mathbf{u}_m = -a_m\nabla p_m$ and assuming that:

$$p_m \in W = L^2(\Omega), \quad \mathbf{u}_m \in \mathbf{V} = \mathrm{H}(\mathrm{div};\Omega),$$

we replace (2) by the equivalent first order variational system:

$$\begin{aligned} &\left(a_m^{-1}\mathbf{u}_m,\mathbf{v}\right)_\Omega - \left(p_m,\nabla\cdot\mathbf{v}\right)_\Omega = -\langle g,\mathbf{v}\cdot\mathbf{n}\rangle_{\partial\Omega},\\ &\left(\nabla\cdot\mathbf{u}_m,w\right)_\Omega = \left(f,w\right)_\Omega, \end{aligned} \tag{4}$$

for any $(\mathbf{v},w)\in(\mathbf{V},W)$, where $(\cdot,\cdot)_D$ and $\langle\cdot,\cdot\rangle_\gamma$ denote inner products on $D\subset\mathbb{R}^2$ and the boundary γ.

We discretize (4) using a Raviart–Thomas mixed finite element scheme [28,29]. We choose the finite element spaces $W_h\subset W$, consisting of the space of piecewise constant functions, and $\mathbf{V}_h\subset\mathbf{V}$, which is the space of vector-valued functions whose x-components are continuous linear in x and discontinuous constant in y and whose y-components are discontinuous constant in x and continuous linear in y. In addition, we apply quadrature to evaluate the integrals in (4). We use subscripts T_x and T_y to denote the trapezoidal quadrature rules in the x and y-direction respectively, subscripts M_x and M_y to denote the midpoint quadrature rules in the x and y-direction respectively, and subscript M to indicate the midpoint approximation on cell edges. Further details about these choices can be found in [18]. The approximation becomes: compute $(\mathbf{u}_{m,h},p_{m,h})\in\mathbf{V}_h\times W_h$ satisfying:

$$\begin{aligned} &\left(a_m^{-1}\mathbf{u}^x_{m,h},\mathbf{v}^x\right)_{T_xM_y} + \left(a_m^{-1}\mathbf{u}^y_{m,h},\mathbf{v}^y\right)_{M_xT_y} - \left(p_{m,h},\nabla\cdot\mathbf{v}\right) = -\langle g,\mathbf{v}\cdot\mathbf{n}\rangle_M,\\ &\left(\nabla\cdot\mathbf{u}_{m,h},w\right) = \left(f,w\right)_{M_xM_y}, \end{aligned} \tag{5}$$

for any $\mathbf{v}\in\mathbf{V}_h, w\in W_h$, where we set $\mathbf{u}_{m,h}=(\mathbf{u}^x_{m,h},\mathbf{u}^y_{m,h}), \mathbf{v}=(\mathbf{v}^x,\mathbf{v}^y)$.

The finite element discretization for a one-dimensional problem is the natural restriction of the two dimensional method. We do not give the discrete formulas here.

2.2.1. Equivalence to the (Ghost Fluid) cell-centered finite volume scheme

If we consider the discrete equations defining the finite element pressure approximation, using p to denote $p_{m,h}$, we obtain:

$$\begin{aligned} &-\Delta y_j\left(a_{m,i+1/2,j}\,\frac{p_{i+1,j}-p_{i,j}}{\Delta x_{i+1/2}} - a_{m,i-1/2,j}\,\frac{p_{i,j}-p_{i-1,j}}{\Delta x_{i-1/2}}\right)\\ &\quad-\Delta x_i\left(a_{m,i,j+1/2}\,\frac{p_{i,j+1}-p_{i,j}}{\Delta y_{j+1/2}} - a_{m,i,j-1/2}\,\frac{p_{i,j}-p_{i,j-1}}{\Delta y_{j-1/2}}\right) = f_{ij}\Delta x_i\Delta y_j, \end{aligned} \tag{6}$$

for $1\leqslant i\leqslant k$, $1\leqslant j\leqslant \ell$, using proper boundary values. These are the discrete equations for the cell-centered finite volume scheme.

2.3. Observations about the hybrid discretization

1. Both the one-and two-dimensional model diffusions are convex interpolants, and hence they preserve any positivity condition placed on the original diffusion constant.
2. The approximation conserves flux across cell boundaries at the cell boundary centers (which is the sense in which standard finite volume methods are conservative) and at cell nodes across diagonals in an average sense if the node does not lie on Γ_d. Indeed, this observation motivate the use of a weighted harmonic average. Assume that a has constant values a^- and a^+ to the left and right side of x_*, see Fig. 2.1. The corresponding values of the flux on either side of the discontinuity are:
$$FLUX^- = -a^-\frac{p_*-p_i}{x_*-x_i} \quad\text{and}\quad FLUX^+ = -a^+\frac{p_*-p_{i+1/2}}{x_{i+1}-x_*},$$
where p_* is the pressure approximation at the discontinuity. To enforce conservation of flux, we equate the two fluxes. Solving the resulting equation yields
$$FLUX^- = -FLUX^+ = -\frac{p_{i+1}-p_i}{\Delta x}\left(\frac{1}{a^-}\frac{x_*-x_i}{\Delta x}+\frac{1}{a^+}\frac{x_{i+1}-x_*}{\Delta x}\right)^{-1},$$
where $\Delta x = x_{i+1}-x_i$. Hence, $a^*_{i+1/2}=\left(\frac{1}{a^-}\frac{x_*-x_i}{\Delta x}+\frac{1}{a^+}\frac{x_{i+1}-x_*}{\Delta x}\right)^{-1}$.
3. In advance of the error analysis below, we note that if a is piecewise constant in one dimension then a_m^{-1} and a^{-1} have the same average value, i.e.
$$\left(a_m^{-1}-a^{-1},1\right)_\Omega = \left(a_m^{-1}-a^{-1},1\right)_{\Omega_d} = 0.$$
Similarly in two dimensions, if a is piecewise constant and Γ_d is a straight line, then we have another equality between the two dimensional integrals of a^{-1} and a_m^{-1} with particular choice of quadratures (see below):
$$\begin{aligned} &\frac{1}{2}\left(a_m^{-1}-a^{-1},1\right)_{\Omega,M_xT_y}+\frac{1}{2}\left(a_m^{-1}-a^{-1},1\right)_{\Omega,M_yT_x}\\ &\quad=\frac{1}{2}\left(a_m^{-1}-a^{-1},1\right)_{\Omega_d,M_xT_y}+\frac{1}{2}\left(a_m^{-1}-a^{-1},1\right)_{\Omega_d,M_yT_x}=0. \end{aligned} \tag{7}$$
4. Because the variational formulation underlying the finite element method involves integrals over the volumes, the finite element approximation is informed by the behavior of the diffusion coefficient in the interior of the volume. Hence, the

finite element approximation "sees" the geometry of the diffusion interface inside each volume. This provides a consistent way to treat different interface geometries.

3. Error analysis

As discussed above, the purpose of the error analysis in this paper is to derive a computational error estimate that produces an accurate estimate of the error in a quantity of interest computed from a particular numerical solution. The estimate accurately quantifies the various contributions to the error, i.e. modeling, discretization, and quadrature. This provides the capability to decide how to improve the discretization if the desired accuracy is not achieved. As we illustrate below with examples, it is crucial to consider error in specific quantities of interest. This is sharply contrasted to the goal of a general *a priori* convergence analysis, which determines the error in a norm.

We present two error estimates. The first is an *a priori* analysis which bounds the effects of introducing a model diffusion coefficient. This is an important component for the main estimate, which is a goal-oriented *a posteriori* estimate on the error in a quantity of interest. The analysis for both results uses the finite element formulation of the method.

3.1. Analysis of the modeling error

We decompose the error in $p_{m,h}$ as

$$e_p = p - p_{m,h} = (p_m - p_{m,h}) + (p - p_m) = e_{p,h} + e_{p,m}. \tag{8}$$

The first error $e_{p,h}$ is the usual approximation error due to numerical discretization and as a consequence of our construction of the modeling problem can be analyzed as in [18]. The second error $e_{p,m}$ estimates the difference between the analytic solutions of the original and model problem. Likewise, we write:

$$e_{\mathbf{u}} = \mathbf{u} - \mathbf{u}_{m,h} = (\mathbf{u}_m - \mathbf{u}_{m,h}) + (\mathbf{u} - \mathbf{u}_m) = e_{\mathbf{u},h} + e_{\mathbf{u},m}. \tag{9}$$

Theorem 3.1. *There is a constant C that depends on $\mathbf{u}$ and a, such that:*

$$\|\mathbf{e}_{\mathbf{u},m}\|_{0,\Omega} \leqslant C\|a^{-1} - a_m^{-1}\|_{0,\Omega}, \tag{10}$$

and

$$\|e_{p,m}\|_{0,\Omega} \leqslant C\|a^{-1} - a_m^{-1}\|_{0,\Omega}. \tag{11}$$

The constant C requires an upper bound on the size of a_m, which does not exceed the size of a if the weighted harmonic average is used to define a_m.

The proof is given in Section A.1. The *a priori* bounds (10) and (11) show that the effects of error introduced by the modeling tend to zero as the mesh is refined. It is possible to be more precise in specific cases. For example, if Γ_d is a straight line of length L and the diffusion is piecewise constant, then it follows that:

$$\|a^{-1} - a_m^{-1}\|_{0,\Omega}^2 \approx O\left(\frac{L}{h}\cdot|a^- - a^+|^2\cdot h^2\right) = O(h), \tag{12}$$

where h is the mesh size and a^- and a^+ are the two values of a. Hence:

$$\|a^{-1} - a_m^{-1}\|_{0,\Omega} = O\left(h^{1/2}\right). \tag{13}$$

That is, the modeling error scales with the square root of the mesh size.

3.2. A goal-oriented a posteriorierror representation

We estimate the total error in a quantity of interest that can be expressed as a linear functional:

$$\mathcal{Q}(p,\mathbf{u}) = (p,\psi_p) + (\mathbf{u},\boldsymbol{\psi}_{\mathbf{u}}),$$

for $\boldsymbol{\psi}_{\mathbf{u}} \in (L^2(\Omega))^2$ and $\psi_p \in L^2(\Omega)$. For this purpose, we require two adjoint problems. The first is associated with the original problem: find $\phi_p \in H^1(\Omega)$ and $\boldsymbol{\phi}_{\mathbf{u}} \in \mathrm{H}(\mathrm{div};\Omega)$ such that:

$$\begin{aligned} &a^{-1}\boldsymbol{\phi}_{\mathbf{u}} - \nabla\phi_p = \boldsymbol{\psi}_{\mathbf{u}}, \quad \text{in } \Omega,\\ &-\nabla\cdot\boldsymbol{\phi}_{\mathbf{u}} = \psi_p, \quad \text{in } \Omega,\\ &\langle\phi_p, \mathbf{v}\cdot\mathbf{n}\rangle = 0, \quad \text{on } \partial\Omega, \quad \forall\ \mathbf{v}\in \mathrm{H}(\mathrm{div};\Omega). \end{aligned} \tag{14}$$

The second is associated with the model problem: find $\phi_{p,m} \in H^1(\Omega)$ and $\boldsymbol{\phi}_{\mathbf{u},m} \in \mathrm{H}(\mathrm{div};\Omega)$ such that:

$$\begin{aligned} &a_m^{-1}\boldsymbol{\phi}_{\mathbf{u},m} - \nabla\phi_{p,m} = \boldsymbol{\psi}_{\mathbf{u}}, \quad \text{in } \Omega,\\ &-\nabla\cdot\boldsymbol{\phi}_{\mathbf{u},m} = \psi_p, \quad \text{in } \Omega,\\ &\langle\phi_{p,m}, \mathbf{v}\cdot\mathbf{n}\rangle = 0, \quad \text{on } \partial\Omega, \quad \forall\ \mathbf{v}\in \mathrm{H}(\mathrm{div};\Omega). \end{aligned} \tag{15}$$

We obtain:

Theorem 3.2 (*A posteriori error representation*). *The error in the quantity of interest is given by*

$$\begin{aligned} (e_p,\psi_p) + (\mathbf{e}_{\mathbf{u}},\boldsymbol{\psi}_{\mathbf{u}}) = \{&-(a_m^{-1}\mathbf{u}_{m,h}, \boldsymbol{\phi}_{\mathbf{u},m} - \Pi_h\boldsymbol{\phi}_{\mathbf{u},m})\\ &+ (f, \phi_{p,m} - \mathbb{P}_h\phi_{p,m}) - \langle g, (\boldsymbol{\phi}_{\mathbf{u},m} - \Pi_h\boldsymbol{\phi}_{\mathbf{u},m})\cdot\mathbf{n}\rangle\}\\ &+ \mathrm{QE1}(\Pi_h\boldsymbol{\phi}_{\mathbf{u},m}) + \mathrm{QE2}(\mathbb{P}_h\phi_{p,m})\\ &- ((a^{-1} - a_m^{-1})\mathbf{u}_m, \boldsymbol{\phi}_{\mathbf{u}}), \end{aligned} \tag{16}$$

where

$$\mathrm{QE1}(\mathbf{v}) = -(a_m^{-1}\mathbf{u}_{m,h},\mathbf{v}) + \left(\left(a_m^{-1}\mathbf{u}_{m,h}^x,\mathbf{v}^x\right)_{T_xM_y} + \left(a_m^{-1}\mathbf{u}_{m,h}^y,\mathbf{v}^y\right)_{M_xT_y}\right) - \langle g,\mathbf{v}\cdot\mathbf{n}\rangle + \langle g,\mathbf{v}\cdot\mathbf{n}\rangle_M, \tag{17}$$

$$\mathrm{QE2}(w) = (f,w) - (f,w)_{M_xM_y}, \tag{18}$$

and Π_h and $\mathbb{P}_h$ denote the lowest order Raviart–Thomas projection and the usual L^2 projection, respectively.

The proof is given in Section A.2. We define the Raviart–Thomas projection in Section A.3.

The first line of (16) estimates the contribution to the error given by the finite element discretization. The second line gives the contribution to the error from using the quadrature that yields the finite volume scheme. Together, the first and second lines give the contribution to the error from discretization of the model problem. The third term $((a^{-1} - a_m^{-1})\mathbf{u}_m, \boldsymbol{\phi}_{\mathbf{u}})$ measures the contribution of modeling error arising because a is replaced by a_m. Note that this term is *not* computable and we deal with that below.

Note that the modeling term integrand is zero outside Ω_d. The term is large if both the modeling error $a^{-1} - a_m^{-1}$ and the adjoint solutions ϕ_p and $\boldsymbol{\phi}_{\mathbf{u}}$ are large in Ω_d. The size of the adjoint solution depends strongly on the location of the support of the function determining the quantity of interest. If we are interested in values far away from the interface, the effect of the modeling on the error will be small, see Fig. 3.1. Moreover, if the adjoint solution is nearly constant in Ω_d, the approximation property of the model for the average value of the diffusion function (7) also leads to a small modeling error contribution.

We note that there are a number of possible finite element + quadrature discretizations that yield different finite volume schemes. The first and second lines of (16) will vary according to the particular approach, for example avoiding the quadrature error expression [25,26].

3.3. A computable a posteriorieestimate

Two approximations are required in (16) in order to obtain a computable *a posteriori* estimate.

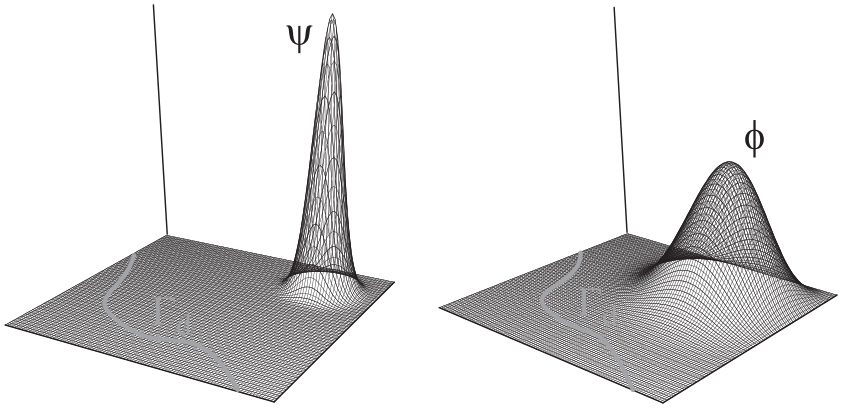

Fig. 3.1. Left: We plot the data ψ that gives the average value in a small region near (.8,.8) in the unit domain. Right: The corresponding adjoint solution for a problem with constant diffusion. Note that the adjoint solution is very near zero along the interface Γ_d. The value of the solution at (.8,.8) will not be heavily affected by the modeling error.

The first is common for this approach, namely we numerically solve the adjoint problem (15) to obtain approximations $\Phi_{p,\,m} \approx \phi_{p,m}$ and $\mathbf{\Phi}_{\mathbf{u},m} \approx \boldsymbol{\phi}_{\mathbf{u},m}$. As a consequence of "Galerkin orthogonality", the approximation of the adjoint problem cannot lie in the finite element space used for the primary problem, see [20,22,18]. Therefore, in order to solve the adjoint problem, we use the second order Raviart–Thomas mixed finite element method on the same mesh used for the primary computation. This insures that the method used to solve the adjoint problem involves the same programming structure as the finite volume scheme for the forward problem. An alternative approach that is widely used is to use a finer mesh for the adjoint solve, see [30]. Determining the optimal approach to solve the adjoint problem for discontinuous interface problems remains to be done.

The second approximation is needed to deal with the unknown modeling solution $\mathbf{u}_m$ and adjoint solution $\boldsymbol{\phi}_{\mathbf{u}}$ in the modeling term $((a^{-1}-a_m^{-1})\mathbf{u}_m, \boldsymbol{\phi}_{\mathbf{u}})$ in (16). We write:

$$\begin{aligned}((a^{-1}-a_m^{-1})\mathbf{u}_m, \boldsymbol{\phi}_{\mathbf{u}}) = &-((a^{-1}-a_m^{-1})\mathbf{u}_{m,h}, \boldsymbol{\phi}_{\mathbf{u},m})\\ &+((a^{-1}-a_m^{-1})\mathbf{u}_{m,h}, \boldsymbol{\phi}_{\mathbf{u},m}-\boldsymbol{\phi}_{\mathbf{u}})\\ &-((a^{-1}-a_m^{-1})(\mathbf{u}_m-\mathbf{u}_{m,h}), \boldsymbol{\phi}_{\mathbf{u}}),\end{aligned}$$

where the first term on the right is computable. We have:

$$\left\|((a^{-1}-a_m^{-1})\mathbf{u}_{m,h}, \boldsymbol{\phi}_{\mathbf{u},m})\right\| \leqslant C\|a^{-1}-a_m^{-1}\| \sim \mathbf{O}\left(h^{1/2}\right),$$

while

$$\begin{aligned}&\left\|((a^{-1}-a_m^{-1})\mathbf{u}_{m,h}, \boldsymbol{\phi}_{\mathbf{u},m}-\boldsymbol{\phi}_{\mathbf{u}}) - ((a^{-1}-a_m^{-1})(\mathbf{u}_m-\mathbf{u}_{m,h}), \boldsymbol{\phi}_{\mathbf{u}})\right\|\\ &\quad\leqslant C\|a^{-1}-a_m^{-1}\|\ \max\left\{\|\mathbf{u}_m-\mathbf{u}_{m,h}\|, \|\boldsymbol{\phi}_{\mathbf{u},m}-\boldsymbol{\phi}_{\mathbf{u}}\|\right\}.\end{aligned}$$

The standard convergence estimate for the finite element discretization and the modeling estimate (10) applied to ϕ suggest that the latter expression is higher order in h than the computable modeling expression. In practice we neglect these terms when computing the estimate. The resulting computable *a posteriori* estimate is

Theorem 3.3 (*Computable A Posteriori error estimate*). *The error in the quantity of interest is approximated by*

$$\begin{aligned}(e_p, \psi_p) + (\mathbf{e}_{\mathbf{u}}, \boldsymbol{\psi}_{\mathbf{u}}) \approx &\left\{-(a_m^{-1}\mathbf{u}_{m,h}, \mathbf{\Phi}_{\mathbf{u},m}-\Pi_h\mathbf{\Phi}_{\mathbf{u},m})\right.\\ &+(f, \Phi_{p,m}-\mathbb{P}_h\Phi_{p,m}) - \langle g, (\mathbf{\Phi}_{\mathbf{u},m}-\Pi_h\mathbf{\Phi}_{\mathbf{u},m})\cdot\mathbf{n}\rangle\}\\ &+\mathrm{QE1}(\Pi_h\mathbf{\Phi}_{\mathbf{u},m}) + \mathrm{QE2}(\mathbb{P}_h\Phi_{p,m})\\ &-((a^{-1}-a_m^{-1})\mathbf{u}_{m,h}, \mathbf{\Phi}_{\mathbf{u},m}).\end{aligned} \tag{19}$$

4. Numerical results

In this section, we present a number of examples to illustrate aspects of the proposed method and error estimate.

4.1. The behavior of a_m as the mesh is refined

We test the properties of the model a_m^{-1} with two problems. These examples verify that the piecewise biquadratic approximation a_m converges to a as the mesh size decreases as determined by (13).

4.1.1. Example 1: discontinuity across a straight line

The discontinuity interface Γ_d is the line $y + 0.45x - 0.73 = 0$. The diffusion coefficient a equals 10^3 on one side of the line and 1 on the other. We plot a_m^{-1} for different mesh sizes in Fig. 4.1. As expected the transition is "smooth" and the region Ω_d decreases with the mesh size.

4.1.2. Example 2: discontinuity across a circle

The discontinuity interface Γ_d is the circle $(x-0.5)^2 + (y-0.5)^2 = 0.4^2$ while the diffusion coefficient a equals 10^3 inside the circle and 1 outside. Plots of a_m^{-1} at different mesh sizes are given in Fig. 4.2. In Fig. 4.2(b), we observe discontinuity in a_m^{-1} at several cell nodes. For this example, we relaxed the continuity condition at a few nodes between cut cells and their neighbors (during step 4 of Algorithm 1) because the center of a neighboring cell on the diagonal actually sits on the interface Γ_d.

4.2. Behavior of the error estimate and the contributions to the error

We present three examples to test the convergence rate of the cut-cell finite volume method, test the accuracy of the error estimate (19), and illustrate the behavior of the contributions to the error as the mesh is refined. A standard way to measure the accuracy of an *a posteriori* error estimate is to use the *effectivity index*:

$$\nu = \frac{\text{Estimated Error}}{\text{Exact Error}}. \tag{20}$$

Ideally, the effectivity index should be one. We study the behavior of ν as the mesh is refined. Note that the modeling problem changes as the mesh is refined since the boundary region Ω_d (on which $a_m \neq a$) changes as the mesh is refined.

4.2.1. Example 3: a one dimensional example

We solve the problem for which the diffusion coefficient is given by

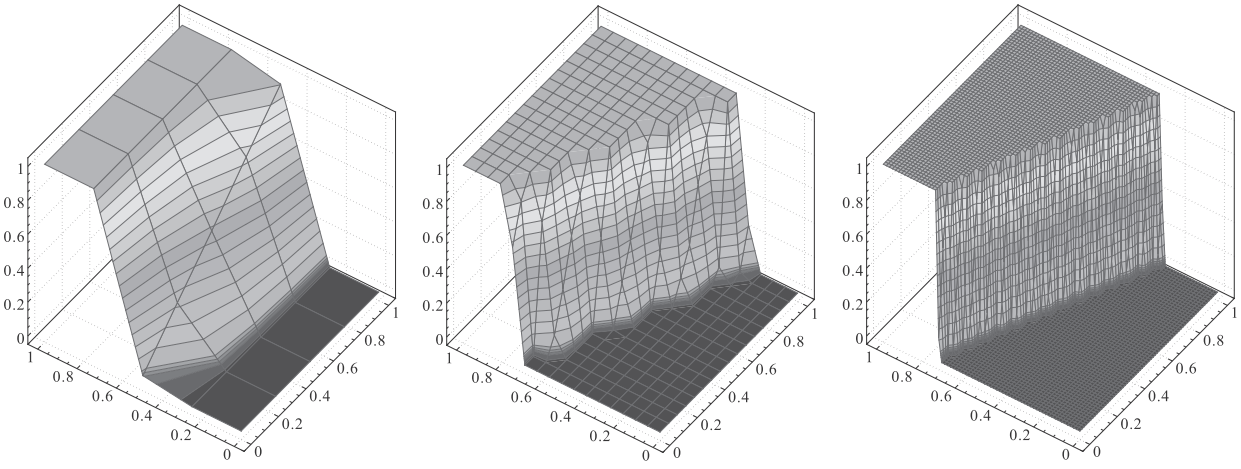

Fig. 4.1. The diffusion is discontinuous across the line $y + 0.45x - 0.73 = 0$. We plot the model diffusion a_m^{-1} for mesh sizes 1/2, 1/8 and 1/32 left to right.

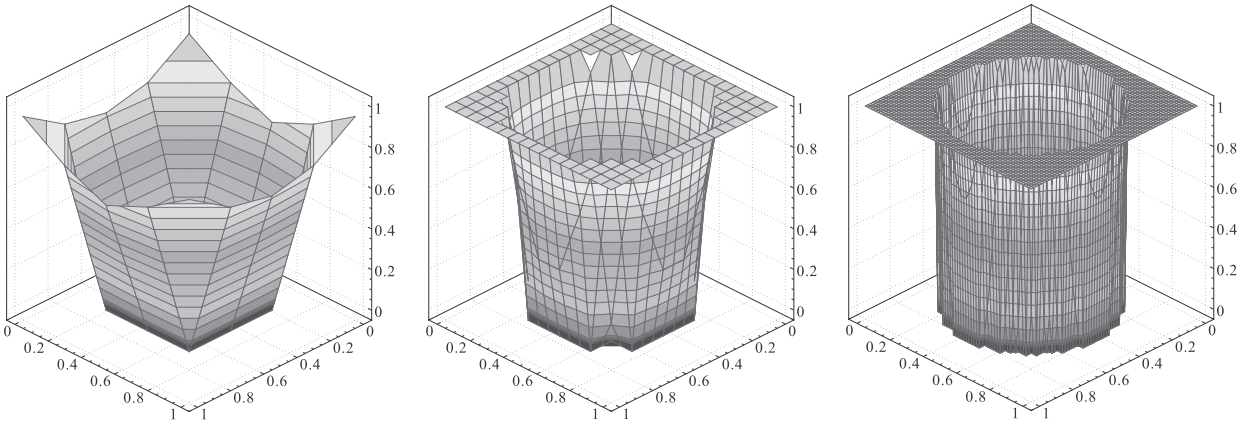

Fig. 4.2. The diffusion is discontinuous across the circle $(x - 0.5)^2 + (y - 0.5)^2 = 0.4^2$. We plot the model diffusion a_m^{-1} for mesh sizes 1/2, 1/8 and 1/32 left to right.

$$a(x) = \begin{cases} 10^{-3}(x+1), & x > 0.45, \\ x+1, & x \leqslant 0.45, \end{cases}$$

with a discontinuity at $x = 0.45$. We set the pressure function to be:

$$p(x) = \begin{cases} 10^3 \sin(x - 0.45) + 2, & x > 0.45, \\ \sin(x - 0.45) + 2, & x \leqslant 0.45, \end{cases}$$

Table 4.1
Example 3: discretization, quadrature and modeling contributions to the error and effectivity indices.

Grid level	v	Discretization	Quadrature	Modeling
(a) Quantity of interest at 0.45				
1	−0.13465	1.6E+00	4.1E+00	−6.0E+00
2	0.24049	−1.4E−01	4.5E−01	−2.6E−01
3	0.78589	−2.7E−02	6.5E−02	−9.5E−03
4	1.09045	−5.1E−03	1.6E−02	−2.6E−03
5	1.02290	−1.3E−03	3.6E−03	−1.9E−04
6	0.97557	−3.3E−04	8.6E−04	3.4E−06
7	0.99520	−8.3E−05	2.2E−04	1.8E−06
(b) Quantity of interest at 0.95				
1	0.93066	7.3E+00	1.1E+01	−5.6E−01
2	1.00957	3.7E+00	3.4E+00	3.3E−02
3	1.00844	5.4E−01	9.5E−01	3.4E−03
4	1.00247	1.2E−01	2.4E−01	−8.1E−05
5	1.00059	2.9E−02	6.1E−02	−2.3E−05
6	0.99998	7.1E−03	1.5E−02	2.9E−06
7	1.00000	1.8E−03	3.8E−03	4.7E−07

and compute the corresponding righthand side $f(x) = -\cos(x - 0.45) + (x + 1)\sin(x - 0.45)$. For a quantity of interest, we take $\boldsymbol{\psi}_{\mathbf{u}} = \mathbf{0}$ and $\psi_p = \exp(-100(x - x_0)^2)$, giving the value of p in a small region centered at a point $x_0 \in [0, 1]$. Effectivity indices and different error contributions corresponding to $x_0 = 0.45$ and $x_0 = 0.95$ are listed in Table 4.1(a) and (b). We record the order of convergence in Table 4.2.

We obtain accurate error estimates on all meshes that are at least modestly refined. Note that the residual and quadrature error contributions at 0.95 are larger than those at 0.45 as a consequence of the larger value of a^{-1} at 0.95 than at 0.45. However, the modeling error contribution for an estimate of the value of the solution at 0.95 is less than that of the modeling error contribution for the value of the solution at 0.45. This indicates that the jump in the

Table 4.2
Example 3: errors and convergence rates.

Grid level	$\|e_p\|_\infty$		$\|e_{\mathbf{u}}\|_\infty$	
	Error	Order	Error	Order
1	5.4E+01	–	2.2E−01	–
2	2.0E+01	1.45	7.0E−02	1.67
3	5.7E+00	1.80	1.9E−02	1.91
4	1.5E+00	1.91	4.6E−03	2.00
5	3.9E−01	1.95	1.2E−03	1.96
6	9.9E−02	1.98	3.0E−04	1.97
7	2.5E−02	1.99	7.6E−05	2.00

diffusion affects the error significantly if the quantity of interest involves values of the solution near the discontinuity.

4.2.2. Example 4: discontinuity across a straight line

Next, we consider a two-dimensional domain where the discontinuity interface Γ_d is the line $y + 0.45x - 0.73 = 0$, with $a = 10^3$ on one side of the line and $a = 1$ on the other. We set the true solution to be:

$$p(x,y) = \begin{cases} 10^{-3}\exp(y + 0.45x - 0.73), \\ \quad y + 0.45x - 0.73 < 0, \\ \exp\left((y + 0.45x - 0.73) - 1 + 10^{-3}\right), \\ \quad y + 0.45x - 0.73 \geqslant 0, \end{cases}$$

and compute the corresponding reaction function f. We test the estimate using three different quantities of interest:

- the average error over the whole domain using $\psi_p = 1$ on $[0,1] \times [0,1]$,
- the average error in a small region close to the discontinuity using $\psi_p = 1$ on $|y + 0.45x - 0.73| \leqslant 0.1$ and $\psi_2 = 0$ otherwise,
- the average error in a small region far away from the discontinuity using $\psi_p = 1$ in $(x - 0.9)^2 + (y - 0.9)^2 \leqslant 0.1^2$ and $\psi_p = 0$ otherwise,

while $\boldsymbol{\psi}_{\mathbf{u}} \equiv \mathbf{0}$ in all three cases.

Effectivity indices and different error contributions are listed in Table 4.3(a)–(c). We record the convergence rates in Table 4.4.

We obtain accurate error estimates on all modestly refined meshes and better for all three quantities of interest. In the case of a quantity of interest localized away from the discontinuous interface Γ_d, we obtain accurate estimates on even crude discretizations. In all cases, the contribution to the error from the modeling is about the same size as the discretization errors. The contributions and the error are significantly smaller for the quantity of interest that is localized away from the discontinuous interface Γ_d. We can explain this by considering the plots of the solutions of the adjoint problems corresponding to the three different quantities of interest, shown in Fig. 4.3. Reflecting the relative sizes of the contributions to the modeling error recorded in Tables 4.3(a)–(c), we see that the effective support of the adjoint solution for the error in a small region far from the discontinuity is relatively localized, which means that modeling has a relatively smaller effect on this quantity of interest. On the other hand, the adjoint solution corresponding to the average error throughout the domain is significantly larger (as is its second derivative, which affects the discretization contribution).

Table 4.3
Example 4: discretization, quadrature and modeling contributions to the error and effectivity indices.

Grid level	ν	Discretization	Quadrature	Modeling
(a) Quantity of interest: average error over the whole domain				
1	1.14635	−2.0E−01	−3.0E−01	6.8E−01
2	1.13430	−3.6E−04	3.3E−02	2.0E−03
3	1.02491	5.1E−03	8.4E−03	−4.9E−03
4	1.12332	−8.0E−04	1.9E−03	1.3E−03
5	0.73218	−2.0E−03	−2.8E−04	2.7E−03
6	0.82330	6.7E−06	−1.4E−05	1.2E−04
7	0.84624	−2.5E−04	−5.2E−05	3.3E−04
(b) Quantity of interest: average error over a small region close to the discontinuity				
1	10.46523	−3.5E−02	−4.6E−02	9.8E−02
2	0.57279	−1.6E−02	1.1E−02	−4.5E−04
3	0.68346	−2.2E−03	3.6E−03	−3.2E−03
4	0.78772	−2.2E−03	8.8E−04	6.9E−04
5	1.34342	−1.4E−03	−6.8E−05	1.2E−03
6	1.16685	−1.0E−04	1.9E−06	4.2E−05
7	1.13166	−1.3E−04	−1.9E−05	1.4E−04
(c) Quantity of interest: average error over a small region remote from the discontinuity				
1	0.85535	2.0E−03	−1.7E−03	1.1E−02
2	0.98893	9.7E−03	1.4E−03	9.1E−05
3	1.02764	2.0E−03	4.4E−04	4.2E−06
4	1.01288	2.5E−04	1.1E−04	−3.0E−07
5	0.95826	−1.5E−05	2.1E−05	1.5E−05
6	0.98716	5.5E−06	5.9E−06	7.7E−07
7	0.97859	−1.6E−06	1.1E−06	2.5E−06

Table 4.4
Example 4: errors and convergence rates.

Grid level	$\|e_p\|_\infty$		$\|e_{\mathbf{u}}\|_\infty$	
	Error	Order	Error	Order
1	1.5E−04	–	1.4E−01	–
2	3.0E−02	−7.68	5.0E−02	1.50
3	1.0E−02	1.56	3.3E−02	0.61
4	3.0E−03	1.76	1.5E−02	1.13
5	8.3E−04	1.86	7.8E−03	0.94
6	2.2E−04	1.91	4.0E−03	0.97
7	5.7E−05	1.94	2.0E−03	0.98

4.2.3. Example 5: Discontinuity across a circle

We consider a discontinuity interface Γ_d equal to the circle of radius 0.4 centered at (0.5,0.5) in the unit square $[0,1] \times [0,1]$. In the interior of the circle the diffusion coefficient is $a = 10^3$ and on the exterior the diffusion coefficient is $a = 1$. We set the pressure to be:

$$p(x,y) = \begin{cases} \exp((x-0.5)^2 + (y-0.5)^2 - 0.16), \\ \quad (x-0.5)^2 + (y-0.5)^2 \leqslant 0.16, \\ 10^3(\exp((x-0.5)^2 + (y-0.5)^2 - 0.16) - 1 + 10^{-3}), \\ \quad (x-0.5)^2 + (y-0.5)^2 > 0.16, \end{cases}$$

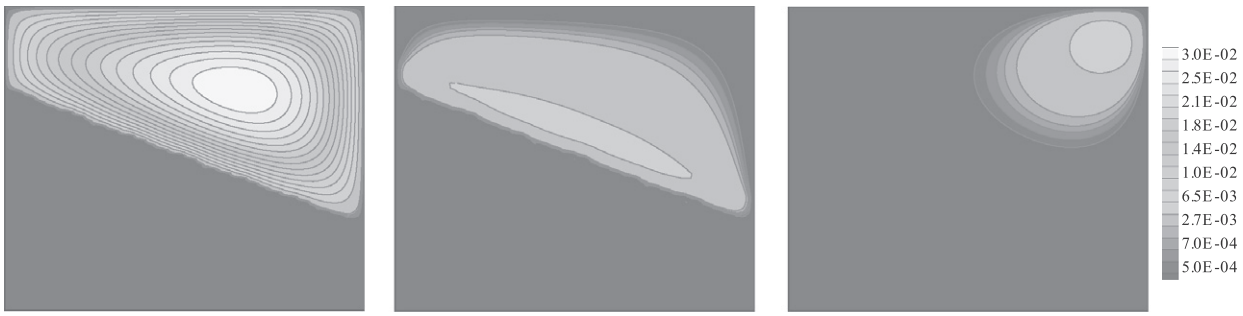

Fig. 4.3. Contour plots of the approximate solutions to the adjoint problems ($\Phi_{p,m}$) in Example 4. From left to right we plot the adjoint solutions corresponding to the quantities of interest: the average error over the whole domain, over a small region close to the discontinuity line and over a small region far from the discontinuity.

Table 4.5
Example 5: discretization, quadrature and modeling contributions to the error and effectivity indices.

Level	ν	Discretization	Quadrature	Modeling
(a) Quantity of interest: average error over the whole domain				
1	1.60932	−7.2E−09	2.0E+02	0.0E+00
2	0.99455	−9.8E+00	1.7E+02	−4.6E+01
3	0.94649	9.6E+00	7.0E+01	−4.0E+01
4	0.81432	2.3E+00	−6.0E+00	−1.3E+00
5	0.64373	5.5E−01	−1.1E−01	1.1E+00
6	1.44595	2.7E+00	2.2E+00	−4.1E+00
7	0.92804	6.5E−02	3.3E−01	−2.5E−01
(b) Quantity of interest: average error over a small region close to the discontinuity				
1	2.55655	−4.6E−09	1.3E+02	0.0E+00
2	1.12078	−1.8E+01	1.1E+02	−3.3E+01
3	0.95507	−3.4E+00	4.8E+01	−2.6E+01
4	0.51732	−1.7E+00	3.8E+00	−6.9E−01
5	0.18757	−5.2E−01	2.3E−02	7.2E−01
6	2.0943	1.4E+00	1.4E+00	−2.5E+00
7	0.83789	−1.4E−02	2.2E−01	−1.6E−01
(c) Quantity of interest: average error over a small region remote from the discontinuity				
1	0.51434	−1.0E−10	2.8E+00	0.0E+00
2	0.92892	2.2E+00	4.8E+00	−3.2E−01
3	1.07235	1.6E+00	1.6E+00	−4.2E−01
4	0.93559	9.9E−03	3.1E−01	2.2E−02
5	0.94296	−5.3E−02	3.8E−02	6.0E−02
6	1.25262	7.4E−03	3.6E−02	−2.5E−02
7	0.78308	−6.9E−03	4.2E−03	4.9E−03

Table 4.6
Example 5: errors and convergence rates.

Grid level	$\|e_p\|_\infty$		$\|e_{\mathbf{u}}\|_\infty$	
	Error	Order	Error	Order
1	5.9E+01	–	5.7E−14	–
2	5.6E+01	0.08	6.0E+01	−49.92
3	2.4E+01	1.21	3.0E+01	1.02
4	7.1E+00	1.77	1.1E+01	1.43
5	1.9E+00	1.89	3.4E+00	1.71
6	5.0E−01	1.95	1.2E+00	1.55
7	1.3E−01	1.98	7.6E−01	0.61

and we compute the corresponding righthand side f. We test using the same three quantities of interest used in Example 4.

The effectivity indices and error contributions for the three different quantities of interest are listed in Table 4.5(a)–(c), respectively. Convergence rates are provided in Table 4.6.

The effectivity ratios are generally acceptable, though still varying significantly on discretization grids at a scale of 64×64. Note that the modeling contributions is estimated to be zero at the initial mesh level, since on the coarse initial mesh the discontinuity lies completely inside the (single) cell and is therefore invisible to the estimate. As before, the contributions to the error and the error are both significantly smaller when the quantity of interest is localized away from the discontinuous interface Γ_d. In this example, we see that the contribution from the modeling error is roughly the same size as the contributions from discretization.

4.2.4. Example 6: distribution of cell contributions to the error

We illustrate the distribution of contributions to the error from the cut-cells and cells in the rest of the domain. In particular, we examine the effect of the curvature in Γ_d on the contribution to the error. We choose Γ_d to be a parabola as shown in the top in Fig. 4.4. The diffusion is 2 on one side of Γ_d and 1 on the other. We estimate the error in the average value over the whole domain.

We first consider a horizontal strip of cells which intersects the discontinuity in two places. The error contributions from each cell are normalized and recorded in the top figure. As expected, the error contributions from cut cells are significantly larger than the error contributions from the cells away from the discontinuity. In the remaining four subplots of Fig. 4.4, we plot the contributions of the cut-cells to the total error and to each of the error components. In particular, Figs. 4.4(a)–(d) show the total error, the modeling error, the residual error, and the quadrature error along the interface respectively. In general, we expect a larger modeling error contribution in a region where the curvature of the discontinuity is larger and all contributions are somewhat larger near the region of highest curvature.

4.2.5. Example 7: the behavior of the estimates in a case with a complex interface

In this example, we study the behavior of the contributions to the error in a problem when the interface Γ_d is rather complicated and the forcing function is not manufactured to produce a given solution. The diffusion coefficient is 10^3 inside a "cross" shaped region in the middle of the unit square and 1 outside. The righthand side f consists of a "source" modeled by a Gaussian function of height 100 near (1,1) and a "sink" modeled by a Gaussian of height-100 near (0,0). The boundary conditions are homogenous Dirichlet. The quantity of interest is the average error in a small region near the source.

We consider both the case when sides of the cross are oriented parallel to the coordinate axis (though not aligned with cell boundaries) and the case when the cross is oriented at an angle with respect to the coordinate axes. The diffusion function for the two cases are plotted in Fig. 4.5. The numerical solutions for the two cases on a 64×64 grid are plotted in Fig. 4.5. The effect of the sudden increase in a can be seen clearly in the solutions.

In Table 4.7, we record the numerical error estimates and the estimated error contributions for a sequence of meshes. For sufficiently fine meshes, the error estimate and the contributions decrease roughly linearly in *log* of mesh size. Refining the mesh leads to a slow improvement in overall accuracy in both cases. The case when the diffusion discontinuity is located along an interface that is oriented at an angle with the axes requires a finer mesh before asymptotic behavior is seen. Note that at the coarsest mesh level, the contribution to the modeling error is estimated as 0 because the discretization does not "see" the discontinuous behavior. The modeling error contributions appear to decrease roughly at a square root rate, ignoring the first two values. We plot this information in Fig. 4.6.

5. Estimating the effect of error in the location of the interface

We carry out a cell-wise *a posteriori* analysis to determine the effects of error in the location of the interface, e.g. arising from experimental measurement or numerical computation. We require the following two "smallness" assumptions to hold.

1. In Ω_d, the intersection points with any line segments connecting the cell centers are in Ω_d, see Fig. 5.1.
2. Location errors do not move the interface Γ_d out of the sub-cells in which it is located in any one realization.

As a special case, we can treat the situation in which the locations are known only for the intersection points with the line segments connecting cell centers through cell boundary centers, see Fig. 5.1. Note that this effectively sets a minimum cell size for a given set of location points.

We suppose that the "true" location of the interface is described by a given set of locations with respect to cell centers $\{\alpha_i h, \beta_i h, \gamma_i h\}$ (see Fig. 5.1). The actual position is determined by the measured

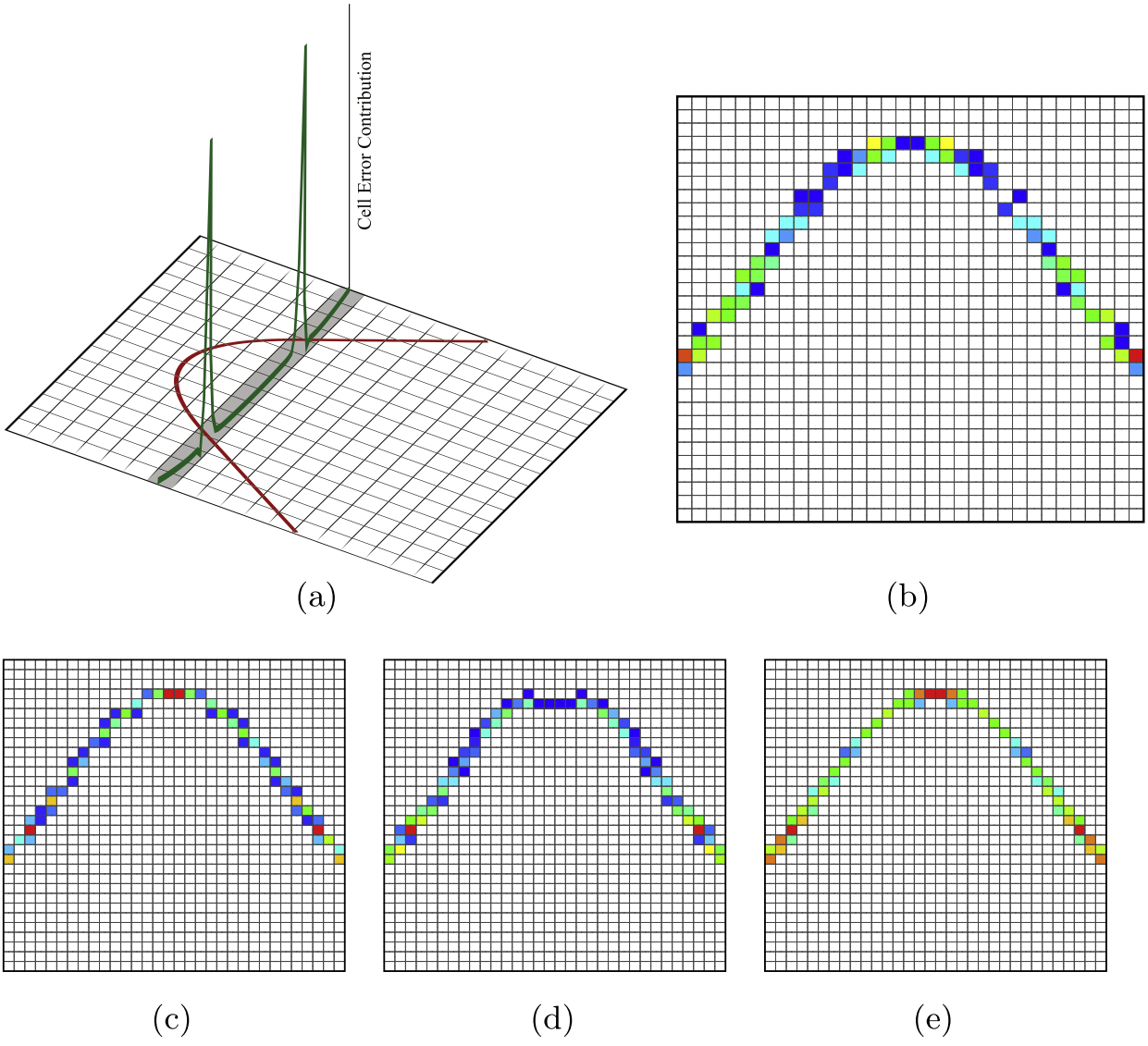

Fig. 4.4. Error distribution test. (a) Cell contributions to the total error in a horizontal strip. The quantity of interest is the average error in the domain. (b)–(e) Error contributions from the cut-cells. (b) Contribution to the total error. Scale: 1.1E−6 to 1.6E−5. (c) Contribution to the modeling error. Scale: 1.4E−6 to 2.1E−6. (d) Contribution to the residual error. Scale: 5.3E−7 to 6.0E−6. (e) Contribution to the quadrature error. Scale: 1.9E−6 to 2.8E−5.

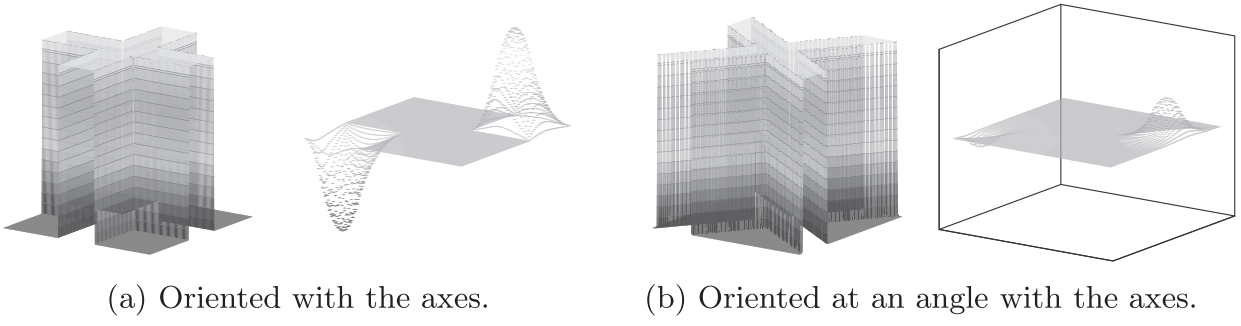

Fig. 4.5. Diffusion coefficients and solutions on a 64 × 64 grid for the two cases in Example 7. The diffusion has value $a = 1000$ inside the cross-shape region and $a = 1$ outside.

or computed values $\{\tilde{\alpha}_i h, \tilde{\beta}_i h, \tilde{\gamma}_i h\}$. We let the corresponding model diffusion values be a_m and $\tilde{a}_m$ respectively. We note that a_m is determined by the coefficients $\{c_1, \ldots, c_9\}$ with respect to the basis for the space of biquadratic functions through an equation of the form:

$$(\text{matrix}) \begin{pmatrix} c_1 \\ \vdots \\ c_9 \end{pmatrix} = b(\{\alpha_i h, \beta_i h, \gamma_i h\}), \tag{21}$$

Table 4.7
Example 7: errors estimates and contributions to the error.

Grid level	Numerical error	Discretization	Quadrature	Modeling
(a) Cross oriented parallel to the axes				
1	−1.4E−01	1.7E−03	−1.4E−01	0.0E+00
2	6.4E−03	5.5E−03	2.9E−03	−2.1E−03
3	−2.1E−03	1.2E−03	−5.3E−03	2.0E−03
4	1.3E−03	1.1E−03	−8.6E−04	1.0E−03
5	5.3E−04	4.6E−04	−5.1E−04	5.7E−04
6	4.7E−04	2.3E−04	−1.5E−04	3.9E−04
7	4.3E−04	1.1E−04	1.1E−04	2.0E−04
(b) Cross oriented at an angle with the axes				
1	2.0E−02	1.4E−02	6.7E−03	0.0E+00
2	4.4E−02	−4.8E−02	6.0E−02	3.4E−02
3	1.9E−02	8.3E−03	1.0E−02	−4.3E−05
4	−8.0E−03	−2.6E−02	7.6E−03	1.1E−02
5	3.7E−04	6.3E−04	−3.2E−04	6.5E−05
6	−1.4E−04	−7.2E−05	−4.6E−04	4.0E−04
7	−7.9E−06	−4.3E−05	−3.3E−05	6.8E−05

where b is a function of the given locations. There is a similar formula for $\tilde{a}_m$. To account for using the measured location rather than the nominal true location, we write the *a posteriori* error estimate as

$$\begin{aligned}\text{error in the estimate} = {} & \text{discretization error}(a_m) \\ & + \text{quadrature error}(a_m) \\ & + \text{modeling error}(a_m - a) \\ & + \text{discretization error}(\tilde{a}_m - a_m) \\ & + \text{quadrature error}(\tilde{a}_m - a_m) \\ & + \text{modeling error}(\tilde{a}_m - a_m),\end{aligned}$$

where the *a posteriori* expressions are evaluated with the indicated diffusion values.

Because of the linear dependence on the diffusion value from (21) we have:

$$(\text{matrix})\begin{pmatrix}\tilde{c}_1 - c_1 \\ \vdots \\ \tilde{c}_9 - c_9\end{pmatrix} = b\left(\left\{\tilde{\alpha}_i h, \tilde{\beta}_i h, \tilde{\gamma}_i h\right\}\right) - b(\{\alpha_i h, \beta_i h, \gamma_i h\}).$$

Note that the new terms in the new estimate can actually be computed independently of the usual estimate, and introducing the location error does not directly impact the computation of the original estimate.

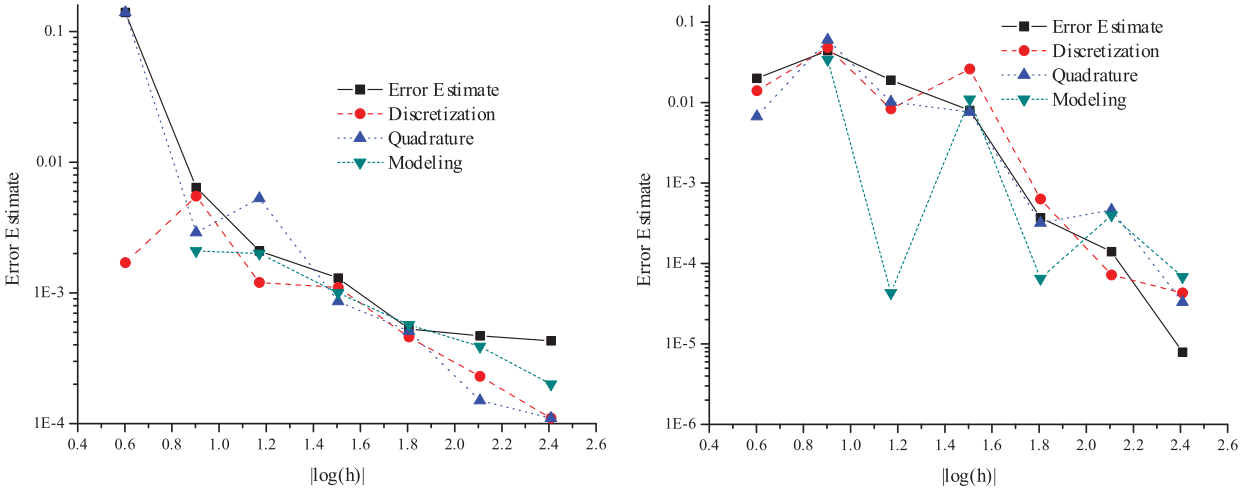

Fig. 4.6. Plots of the absolute values of the error estimate and contributions to the error versus *log* mesh size. Left: cross is oriented parallel to the coordinate axes. Right: cross is oriented diagonally to the coordinate axes. Note: the error estimate is computing using the *signed* contributions and cancellation can result in the estimate being smaller than any of the contributions, as illustrated on the right.

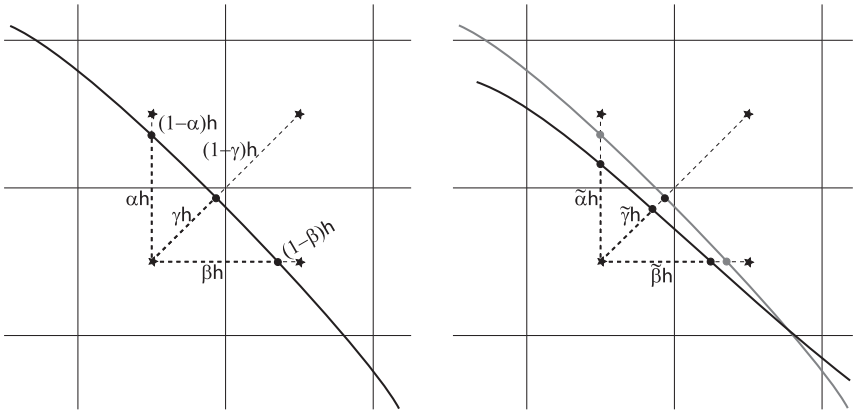

Fig. 5.1. Left: We locate the interface with respect to the discretization using the positions along line segments connecting cell centers. Right: The notation for the actual measured or computed position.

For simplicity, we compute the difference $\tilde{a}_m - a_m$ on a unit square $[0,1]\times[0,1]$ with center at $x_0 = (0.5, 0.5)$. We denote the differences in a^{-1} between x_0 and the other three neighbor cell centers along αh, βh and γh as r, s and t, see Fig. 5.1. We also denote $\Delta\alpha = \alpha - \tilde{\alpha}, \Delta\beta = \beta - \tilde{\beta}$ and $\Delta\gamma = \gamma - \tilde{\gamma}$. Using the basis $\{1, x, y, xy, x^2, x^2y, x^2y^2, y^2, xy^2\}$, we compute and obtain the error between a_m and $\tilde{a}_m$ as follows:

$$\begin{aligned} a_m - \tilde{a}_m = {} & (-4\Delta\alpha\, r - 4\Delta\beta\, s + \Delta\gamma)\, xy + (4\Delta\alpha\, r + 8\Delta\beta\, s - 2\Delta\gamma)\, x^2y \\ & + (8\Delta\alpha\, r + 4\Delta\beta\, s - 2\Delta\gamma)\, xy^2 \\ & + (-8\Delta\alpha\, r - 8\Delta\beta\, s + 4\Delta\gamma)\, x^2y^2. \end{aligned}$$

Note that the first term containing xy is the leading order term. The discrepancy is exaggerated by both the jump in diffusion across the discontinuity and the perturbation along various directions. Quantification of this error sets a minimum cell size for a given set of location points and provides a criteria on the reliability of the experimental measurement of discontinuity locations.

6. Conclusion

In this paper, we discuss the modeling and accurate simulation of a diffusive process in a domain consisting of two distinct materials with different material properties. We assume that the diffusion value changes discontinuously across a smooth interface curve interior to the domain of the system, while we require that the solution be continuous and have a continuous normal flux across the interior interface boundary. In a regular discretization of the domain, the interface "cuts" through the cells (elements or volumes) without respecting the regular geometry of the discretization, yielding a "cut-cell" problem. Consequently, the discontinuity in the diffusion coefficients has a strong impact on the accuracy and convergence of the numerical method. The first goal of this paper is to describe a systematic approach to discretizing a cut-cell problem that handles complex geometry in the interface in a natural fashion while yielding reliable accuracy and stability. The method uses a hybrid modeling-discretization approach based on the well-known equivalence between mixed finite element methods employing special basis functions and quadrature formulas and cell-centered finite volume methods. Next, we carry out an *a posteriori* error analysis for the numerical solution for the error in a quantity of interest that accounts for both the modeling error arising from the replacement of the diffusion coefficient by a new model coefficient and a discretization error arising from the subsequent finite element/finite volume discretization. We test the accuracy of the estimates in a series of examples.

The approach used in this paper is also applicable to problems in which the diffusion coefficient a varies in scale as well as being discontinuous. We intend to pursue this problem in future research.

Acknowledgements

Estep's work is supported in part by the Defense Threat Reduction Agency (HDTRA1-09-1-0036); Department of Energy (DE-FG02-04ER25620, DE-FG02-05ER25699, DE-FC02-07ER54909, DE-SC0001724); Lawrence Livermore National Laboratory (B573139, B584647); the National Aeronautics and Space Administration (NNG04GH63G); the National Science Foundation (DMS-0107832, DMS-0715135, DGE−0221595003, MSPA-CSE−0434354, ECCS-0700559); Idaho National Laboratory (00069249); and the Sandia Corporation (PO299784). Tavener's work is supported in part by the Department of Energy (DE-FG02-04ER25620).

Appendix A. Proofs

A.1. Proof of Theorem 3.1

We derive an error estimate using the mixed weak formulation. Denote $\mathbf{u}$ and p satisfy:

$$(a^{-1}\mathbf{u}, \mathbf{v})_\Omega - (p, \nabla\cdot\mathbf{v})_\Omega = -\langle g, \mathbf{v}\cdot\mathbf{n}\rangle_{\partial\Omega}, (\nabla\cdot\mathbf{u}, w)_\Omega = (f, w)_\Omega, \quad (22)$$

for any $(\mathbf{v}, w) \in (\mathbf{V}, W)$. Subtracting the equations in (4) from those in (22), we get:

$$(a_m^{-1}\mathbf{e}_{\mathbf{u},m}, \mathbf{v}) - (e_{p,m}, \nabla\cdot\mathbf{v}) = -\big((a^{-1} - a_m^{-1})\mathbf{u}, \mathbf{v}\big), (\nabla\cdot\mathbf{e}_{\mathbf{u},m}, w) = 0, \quad (23)$$

where, in the first equation, we insert $\pm(a_m^{-1}\mathbf{u}, \mathbf{v})$. Since $\nabla\cdot\mathbf{e}_{\mathbf{u},m} \in W$, we take $w = e_{p,m}$ and conclude that $(\nabla\cdot\mathbf{e}_{\mathbf{u},m}, e_{p,m}) = 0$. We now take $\mathbf{v} = \mathbf{e}_{\mathbf{u},m}$ in the first equation and obtain (10).

In order to estimate $e_{p,m}$, we use a duality argument. Consider the adjoint problem for $\phi \in H_0^1(\Omega)$:

$$\begin{aligned} & -\nabla\cdot(a_m\nabla\phi) = \psi, \quad \text{on } \Omega, \\ & \phi = 0, \quad \text{on } \partial\Omega, \end{aligned} \quad (24)$$

for $\psi \in L^2(\Omega)$. We have:

$$\begin{aligned} (e_{p,m}, \psi) &= \big(e_{p,m}, -\nabla\cdot(a_m\nabla\phi)\big) \\ &= -\big((a^{-1} - a_m^{-1})\mathbf{u}, a_m\nabla\phi\big) - \big(a_m^{-1}\mathbf{e}_{\mathbf{u},m}, a_m\nabla\phi\big), \end{aligned}$$

where we use (23). Taking $\psi = e_{p,m}$, we obtain:

$$\begin{aligned} \|e_{p,m}\|_{0,\Omega}^2 &\le C\Big\{\|a^{-1} - a_m^{-1}\|_{0,\Omega} + \|\mathbf{e}_{\mathbf{u},m}\|_{0,\Omega}\Big\}\|a_m\nabla\phi\|_{0,\Omega} \\ &\le C\|a^{-1} - a_m^{-1}\|_{0,\Omega}\|e_{p,m}\|_{0,\Omega}. \end{aligned}$$

In the last inequality, we use (10) and the regularity of the elliptic problem.

Hence, we obtain (11).

A.2. Proof of Theorem 3.2

Since $e_p = e_{p,m} + e_{p,h}$, and $\mathbf{e}_{\mathbf{u}} = \mathbf{e}_{\mathbf{u},m} + \mathbf{e}_{\mathbf{u},h}$, the error in the quantity of interest satisfies:

$$\begin{aligned} (e_p, \psi_p) + (\mathbf{e}_{\mathbf{u}}, \boldsymbol{\psi}_{\mathbf{u}}) = {} & \big\{(e_{p,m}, \psi_p) + (\mathbf{e}_{\mathbf{u},m}, \boldsymbol{\psi}_{\mathbf{u}})\big\} \\ & + \big\{(e_{p,h}, \psi_p) + (\mathbf{e}_{\mathbf{u},h}, \boldsymbol{\psi}_{\mathbf{u}})\big\}. \end{aligned} \quad (25)$$

For the discretization errors, $e_{p,h}$ and $\mathbf{e}_{\mathbf{u},h}$, we have the error equations:

$$(a_m^{-1}\mathbf{e}_{\mathbf{u},h}, \mathbf{v}) - (e_{p,h}, \nabla\cdot\mathbf{v}) = \mathrm{QE1}\ (\mathbf{v}), \quad \forall\ \mathbf{v} \in V_h, \quad (26a)$$

$$(\nabla\cdot\mathbf{e}_{\mathbf{u},h},\ w) = \mathrm{QE2}\ (w), \quad \forall\ w \in W_h. \quad (26b)$$

The second term of (25) in curl bracket can be estimated using the arguments in [18], yielding:

$$\begin{aligned} (e_{p,h}, \psi_p) + (\mathbf{e}_{\mathbf{u},h}, \boldsymbol{\psi}_{\mathbf{u}}) = {} & \big\{-(a_m^{-1}\mathbf{u}_{m,h}, \boldsymbol{\phi}_{\mathbf{u},m} - \Pi_h\boldsymbol{\phi}_{\mathbf{u},m}) \\ & + (f, \phi_{p,m} - \mathbb{P}_h\phi_{p,m})\big\} \\ & - \langle g, (\boldsymbol{\phi}_{\mathbf{u},m} - \Pi_h\boldsymbol{\phi}_{\mathbf{u},m})\cdot\mathbf{n}\rangle + \mathrm{QE1}(\Pi_h\boldsymbol{\phi}_{\mathbf{u},m}) \\ & + \mathrm{QE2}(\mathbb{P}_h\phi_{p,m}). \end{aligned} \quad (27)$$

To estimate the modeling errors $e_{p,m}$ and $\mathbf{e}_{\mathbf{u},m}$, we use the adjoint problem (14). Arguing as in the treatment of (23), we obtain:

$$\begin{aligned} (e_{p,m}, \psi_p) + (\mathbf{e}_{\mathbf{u},m}, \boldsymbol{\psi}_{\mathbf{u}}) &= \big(e_{p,m}, -\nabla\cdot\boldsymbol{\phi}_{\mathbf{u}}\big) + \big(\mathbf{e}_{\mathbf{u},m}, a^{-1}\boldsymbol{\phi}_{\mathbf{u}} - \nabla\phi_p\big) \\ &= \big\{-(e_{p,m}, \nabla\cdot\boldsymbol{\phi}_{\mathbf{u}}) + (a^{-1}\mathbf{e}_{\mathbf{u},m}, \boldsymbol{\phi}_{\mathbf{u}})\big\} \\ &\quad + (\nabla\cdot\mathbf{e}_{\mathbf{u},m}, \phi_p) = -\big((a^{-1} - a_m^{-1})\mathbf{u}_m, \boldsymbol{\phi}_{\mathbf{u}}\big). \end{aligned} \quad (28)$$

Combining (27) and (28), we get an error representation (16).

A.3. Definition of the Raviart–Thomas projection

We first denote:

$$P_{k1,k2}(K) = \left\{ p(x,y) = \sum_{i\leqslant k1, j\leqslant k2} c_{ij}\, x^i\, y^j, \quad (x,y)\in K, \quad c_{ij}\in\mathbb{R} \right\},$$

for $K \in \Omega_h$. Then the kth order Raviart–Thomas space is

$$\mathbf{V}^k_{\mathrm{RT}}(K) = P_{k+1,k}(K) \times P_{k,k+1}(K).$$

The kth order Raviart–Thomas projection $\Pi_h : \mathbf{V}|_K \mapsto \mathbf{V}^k_{\mathrm{RT}}(K)$ is, for $\mathbf{v} \in \mathbf{V}|_K$:

$$\langle (\Pi_h \mathbf{v} - \mathbf{v})\cdot \mathbf{n},\ z\rangle_e = 0, \quad \forall\, z \in \mathcal{P}^k(e), \quad \forall\, e \in \partial K, \tag{29a}$$

$$(\Pi_h \mathbf{v} - \mathbf{v}, \boldsymbol{\eta})_K = 0, \quad \forall\, \boldsymbol{\eta} \in \mathbf{V}^{k-1}_{\mathrm{RT}}(K), \tag{29b}$$

where $\mathcal{P}^k(e)$ denotes the space of polynomials of orders up to k on edge e. The approximation properties of the Raviart–Thomas projection can be found in [29].

References

[1] X. Liu, R. Fedkiw, M. Kang, A boundary condition capturing method for Poisson's equation on irregular domains, J. Comput. Phys. 160 (2000) 151–178.
[2] X. Liu, T. Sideris, Convergence of the ghost fluid method for elliptic equations with interfaces, Math. Comput. 72 (244) (2003) 1731–1746.
[3] R. Lebas, T. Menard, P.A. Beau, A. Berlmont, F.-X. Demoulin, Numerical simulation of primary break-up and atomization: DNS and modelling study, Int. J. Multiphas. Flow 35 (2009) 247–260.
[4] G. Luret, T. Menard, A. Berlmont, J. Reveillon, F.-X. Demoulin, G. Blokeel, Modeling collision outcome in moderately dense sprays, Atomization Sprays 20 (2010) 251–268.
[5] E. Bjorklund, The level-set method applied to droplet dynamics in the presence of an electric field, Comput. Fluids 38 (2009) 358–369.
[6] P.M. Young, K. Mohseni, Force characterization of dielectrophoresis in droplet transport, in: S.S. Sadhal (Ed.), Interdisciplinary Transport Phenomena: Fluid, Thermal, Biological, Materials, and Space Sciences, Blackwell Publishing, Oxen, England, 2009.
[7] D. He, H. Huang, Y. Tan, Numerical simulation for a droplet fission process of electrowetting of dielectric device, Commun. Comput. Phys. 7 (2010) 1076–1094.
[8] X. Wang, T.L. Jackson, L. Massa, Numerical simulation of heterogeneous propellant combustion by a level set method, Combust. Theor. Model. 8 (2004) 227–254.
[9] X. Wang, K. Hossain, T.L. Jackson, The three-dimensional numerical simulation of aluminized composite solid propellant combustion, Combust. Theor. Model. 12 (2008) 45–71.
[10] D.Q. Nguyen, R. Fedkiw, M. Kang, A boundary capturing method for incompressible flame discontinuties, J. Comput. Phys. 172 (2001) 71–98.
[11] S. Tanguy, T. Menard, A. Berlemont, A level set method for vaporizing two-phase flows, J. Comput. Phys. 221 (2007) 837–853.
[12] S.P. van der Pijl, A. Segal, C. Vuik, P. Wesseling, A mass-conserving level-set method for modelling of multi-phase flows, Int. J. Numer. Methods Fluids 47 (2005) 339–361.
[13] D. Munger, A. Vincent, Electric boundary conditions at the anodes in aluminum reduction cells, Metall. Mater. Trans. B Proc. Metall. Mater. Proc. Sci. 37 (2006) 1025–1035.
[14] O. Song, D. Kim, H.-S. Ko, Derivative particles for simulating detailed movements of fluids, IEEE Trans. Vis. Comput. Graph. 13 (2007) 711–719.
[15] N. Kang, J. Park, J. Noh, S.Y. Shin, A hybrid approach to multiple fluid simulation using volume fractions, Comput. Graph. Forum 29 (2010) 685–694.
[16] J.A. Sethian, P. Smereka, Level set methods for fluid interfaces, Annu. Rev. Fluid Mech. 35 (2003) 341–372.
[17] M.J. Aftosmis, M.J. Berger, J.E. Melton, Robust and efficient Cartesian mesh generation for component-based geometry, AIAA Paper 97–0196.
[18] D. Estep, M. Pernice, S. Tavener, D. Pham, H. Wang, A posteriori error analysis of a cell centered finite volume method for semilinear elliptic problems, J. Comput. Appl. Math. 233 (2009) 459–472.
[19] R. Becker, R. Rannacher, An optimal control approach to a posteriori error estimation in finite element methods, Acta Numer. (2001) 1–102.
[20] K. Eriksson, D. Estep, P. Hansbo, C. Johnson, Introduction to adaptive methods for differential equations, in: Acta Numerica, 1995, Acta Numer., Cambridge University Press, Cambridge, 1995, pp. 105–158.
[21] K. Eriksson, D. Estep, P. Hansbo, C. Johnson, Computational Differential Equations, Cambridge University Press, Cambridge, 1996.
[22] D. Estep, M.G. Larson, R.D. Williams, Estimating the error of numerical solutions of systems of reaction-diffusion equations, Mem. Am. Math. Soc. 146 (696) (2000). viii+109.
[23] M. Giles, E. Süli, Adjoint methods for PDEs: a posteriori error analysis and postprocessing by duality, Acta Numer. (2002) 145–236.
[24] T.F. Russell, M.F. Wheeler, Finite element and finite difference methods for continuous flows in porous media, in: R.E. Ewing (Ed.), The Mathematics of Reservoir Simulation, SIAM, Philadelphia, 1983.
[25] A. Younes, P. Ackerer, G. Chavent, From mixed finite elements to finite volumes for elliptic PDEs in two and three dimensions, Int. J. Numer. Methods Engrg. 59 (2004) 365–388.
[26] M. Vohralik, Equivalence between lowest-order mixed finite element and multi-point finite volume methods on simplicial meshes, M2AN Math. Model. Numer. Anal. 40 (2006) 367–391.
[27] Z. Li, An overview of the immersed interface method and its applications, Taiwan. J. Math. 7 (2003) 1–49.
[28] T. Arbogast, M. Wheeler, I. Yotov, Mixed finite elements for elliptic problems with tensor coefficients as cell-centered finite differences, SIAM J. Numer. Anal. 34 (1997) 828–852.
[29] F. Brezzi, M. Fortin, Mixed and Hybrid Finite Element Methods, Springer-Verlag, New York, 1991.
[30] W. Bangerth, R. Rannacher, Adaptive Finite Element Methods for Differential Equations, Birkhauser-Verlag, 2003.